Science Advances

Supplementary Materials for

THz induced giant spin and valley currents

Sangeeta Sharma *et al*.

Corresponding author: Sangeeta Sharma, sharma@mbi-berlin.de; Samuel Shallcross, shallcross@mbi-berlin.de

This PDF file includes:

Sections S1 to S5
Figs. S1 to S13

1 Decoherence

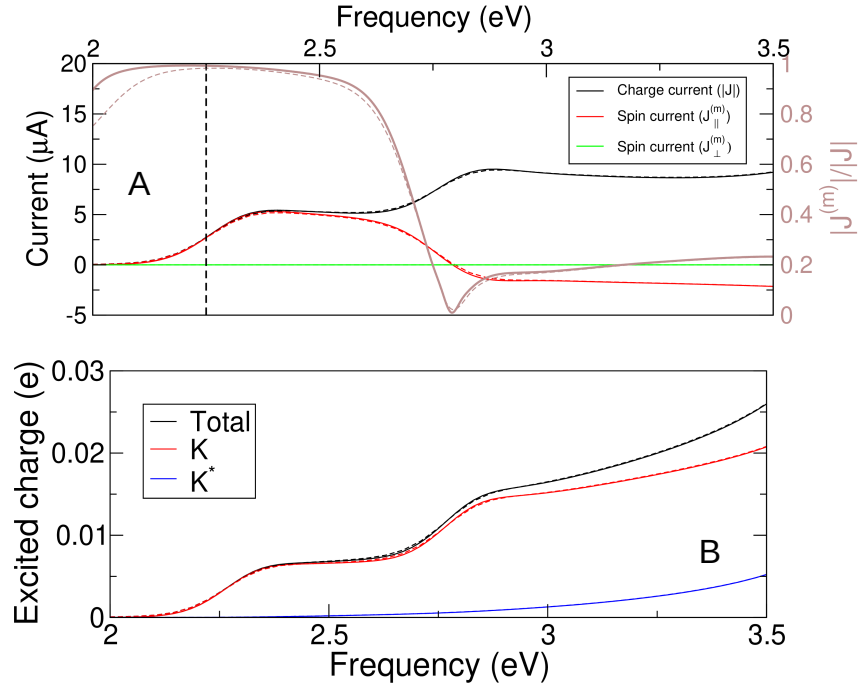## 1.1 Impact of decoherence in tungsten diselenide spin/valley currents

Figure S1: **Valley current control by hencomb pulse of varying frequency both with (full lines) and without (dashed lines) including the effects of decoherence**. The vector potential amplitudes are 0.69 a.u. and 10.96 a.u. for the circularly polarized and THz components respectively with both components having a full width half maximum 14.5 fs. In panel A is shown, as indicated in the caption, both the spin current parallel ($J_{\parallel}^{(m)}$) to the direction of the linearly polarized THz pulse as well as the perpendicular spin current ($J_{\perp}^{(m)}$), along with the total charge current $|J|$. The left hand axis refers to the ratio of spin to charge currents, $|J_{\parallel}^{(m)}|/|J|$, which is seen to be close to 1 from frequencies tuned to the gap of 2.25 eV. There is almost no impact on the results by including the effects of decoherence ($t_D = 200$ fs), with the only notable change being to reduce the value of $|J_{\parallel}^{(m)}|/|J|$ for below gap frequencies in which very little charge is excited, see the excited charge at K and K* as displayed in the panel B.
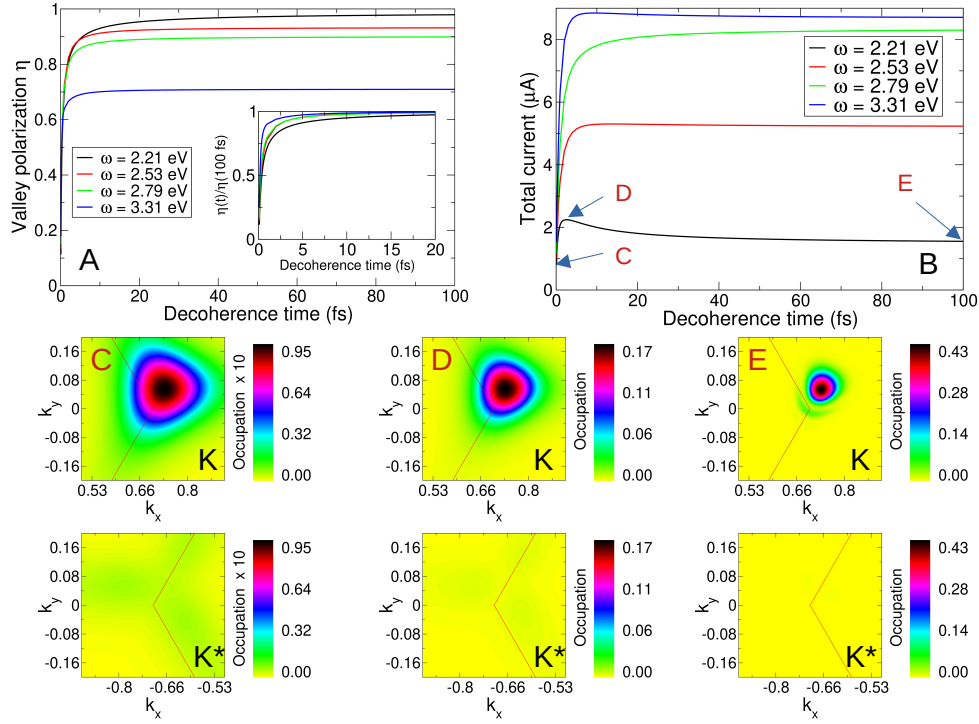
Figure S2: **Dependence of, panel A, valley polarization η and, panel B, the total current on the decoherence (i.e. dephasing) time T_D in WSe$_2$**. Only for $T_D < 5$ fs is substantial degradation of valley purity seen. While dephasing always results in a decrease in valley contrast, it can generate an increase in current at the charge population exited by the hencomb pulse is smeared out to higher momenta, as shown in panels C-E that display the momentum resolved excitation for three dephasing times as indicated in panel B. The full width half maxima of the THz and circularly polarized pulse components are 14.5 fs; the vector potential amplitudes 10.96 and 0.69 a.u. respectively; while the peak electric field and peak power density are 3.3 MV/cm and $10^{1}0$ W/cm^2.

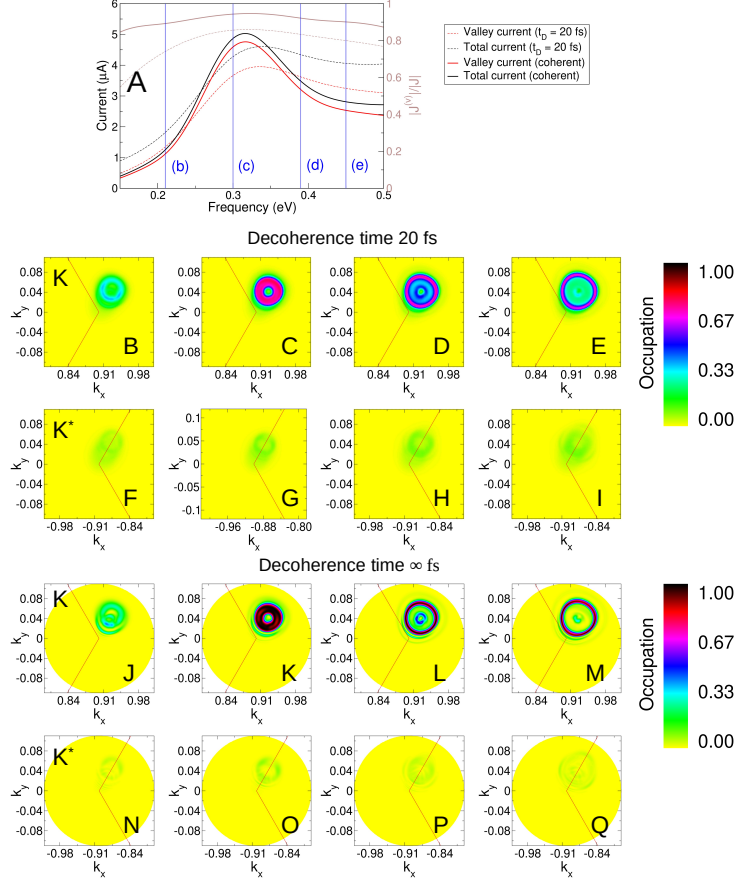## 1.2 Impact of decoherence in bilayer graphene valley currents

Figure S3: **Impact of decoherence on the valley current generated by a hencomb pulse in bilayer graphene, with an interlayer bias of 0.2 eV**. (The corresponding band structure is shown in Fig. 4 of the main manuscript). The valley current and total current are shown in panel A for coherent dynamics (full lines) and with the effects of decoherence (dashed lines). The effect of decoherence is to somewhat reduce the valley purity of the current response, as can be noted from the $\sim 10\%$ reduction in the plot of the ratio of valley to total current, $|J^{(v)}|/|J|$ referred to the left hand side axis. Corresponding momentum space resolved charge excitations at the K and K* valleys for four representative frequencies, as indicated in panel A, are displayed in panels B-I, including the effects of decoherence, and panels J-Q, coherent dynamics. The full width half maxima of the THz and circularly polarized pulse components are 23.5 fs and 49.5 fs; the vector potentials 0.69 a.u. and 6.85 a.u.; the maximal values of the peak power density and peak electric field are 5.8×10^8 W/cm^2 and 0.68 MV/cm.
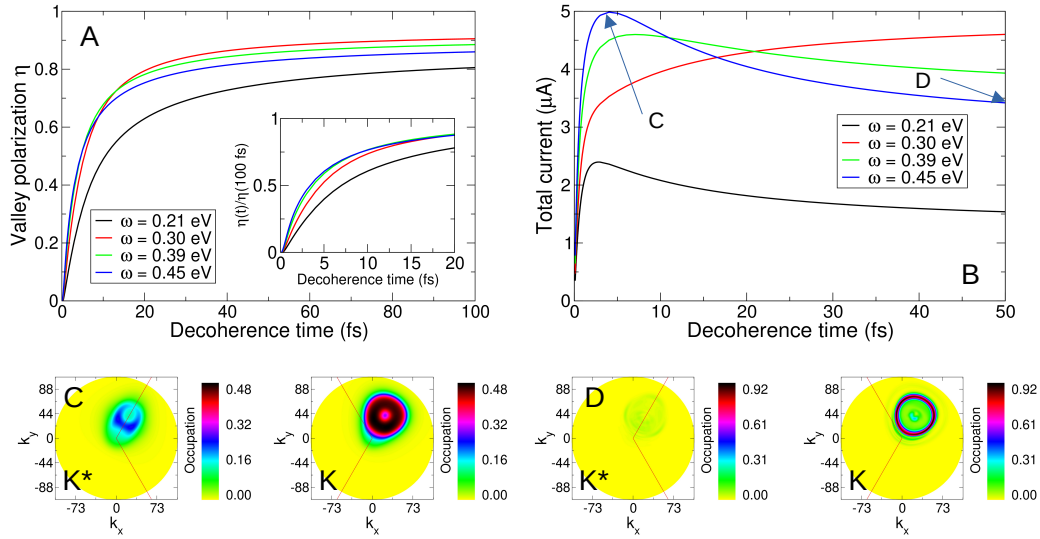
Figure S4: **Dephasing physics in bilayer graphene**. Panel A: Dependence of valley polarization η on the dephasing time T_D in bilayer graphene with a gap of 0.3 eV. For for $T_D < 20$ fs (see inset) substantial degradation of valley purity is seen, such that a 5 fs decoherence (i.e. dephasing) time generates only approximately 50% valley polarization. Panel B: While dephasing always results in a decrease in valley contrast, it can generate an increase in the total current as the charge population exited by the hencomb pulse is smeared out to higher momenta, as can be seen by comparing panels C and D that display the momentum resolved excitation for three decoherence (i.e. dephasing) times as indicated in panel B. The full width half maxima of the THz and circularly polarized pulse components are 23.5 fs and 49.5 fs; the vector potential amplitudes 0.69 a.u. and 6.9 a.u.; the peak electric field and power density are 0.34 MV/cm and 10^8 W/cm^2.
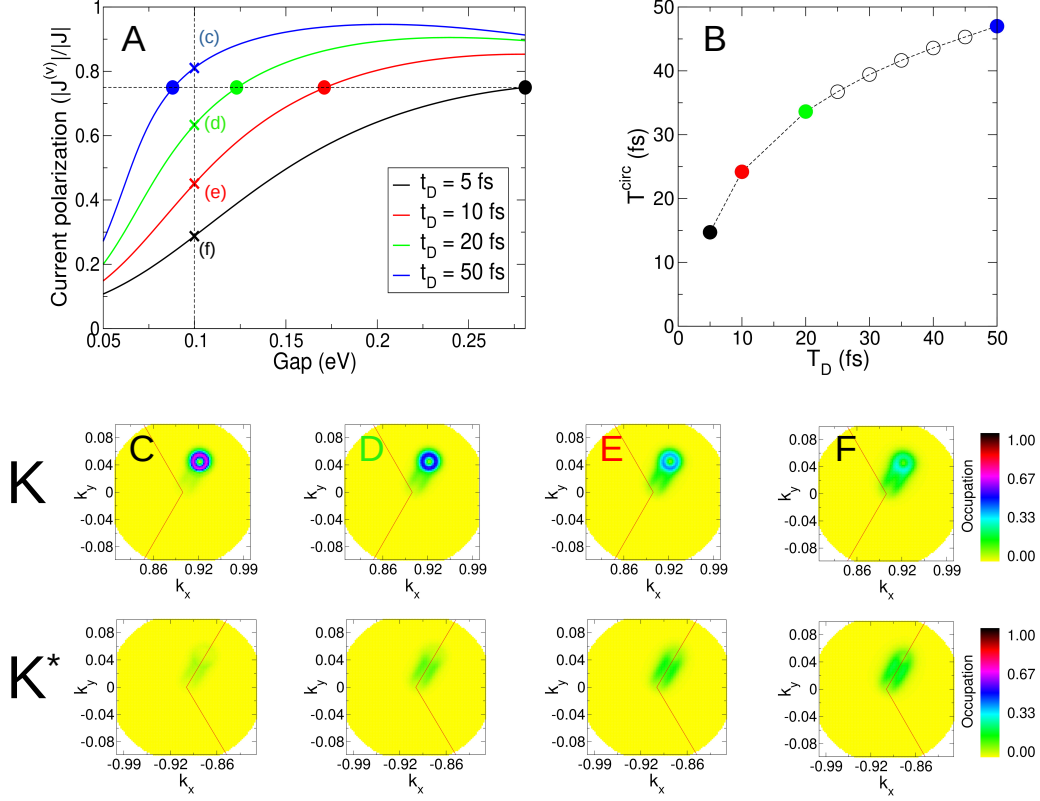
Figure S5: **Impact of current polarization of the interplay between dephasing time and gap size in biayer graphene**. Panel A: Dependence upon the gap of bilayer graphene of the valley polarization ($|J^{(v)}|/|J|$) of the current induced by a hencomb pulse ($J^{(v)}$ is defined as the difference in the two currents obtained by integrating over currents in each of the conjugate valleys). Shown are the results for four dephasing times as indicated by the caption. The filled circles correspond to the value of the gap at which the valley polarization falls below 75% for each dephasing time; in panel B these points are shown with the gap expressed as the time period T^{circ} of corresponding gap tuned circularly polarized light. The vertical line corresponds to a gap of 100 meV, and in panels C-F are shown the momentum resolved excitation corresponding to the points labeled in panel A. As can be seen, increasing the dephasing time leads to a smearing out of the charge excitation and, simultaneously, a loss of valley contrast. The full width half maximum of the THz and circularly polarized components are 211.9 fs and 23.5 fs respectively; the vector potential amplitudes 6.85 a.u. and 0.69 a.u.; and the peak electric field and power density 0.076 MV/cm and 5.8×10^7 W/cm^2.

2 Robustness of the hencomb pulse current response

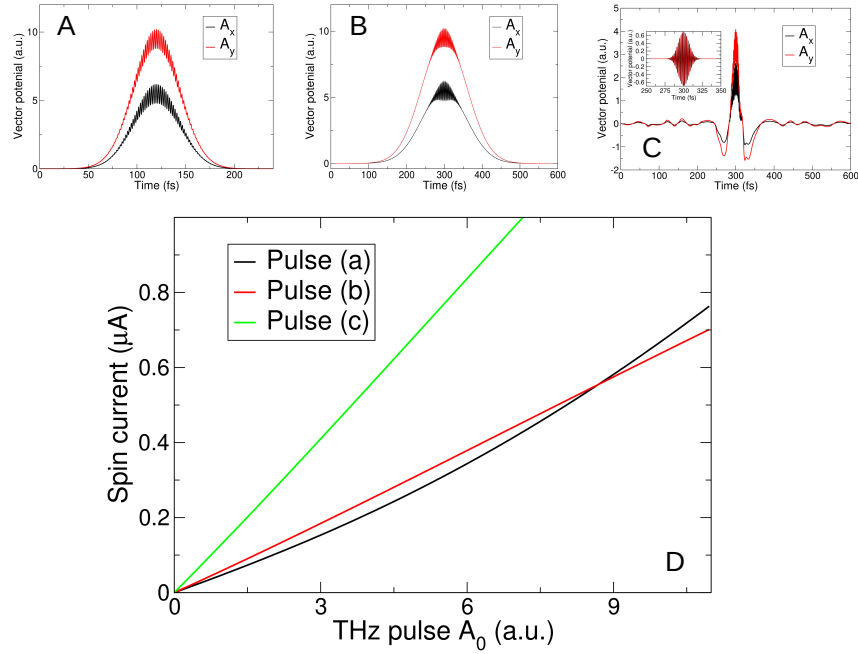## 2.1 Variation of hencomb pulse type: example of WSe$_2$

Figure S6: **Spin current generated by three distinct hencomb pulses**. The pulses in panels A and B have significantly increased duration while in panel C the THz waveform has been directly taken from experiment, Fig. 24 of Ref. 29. The inset in panel C represents the circularly polarized waveform added to the experimental THz envelope to create the "hencomb" pulse. Panel D: Spin current generated in WSe$_2$ as a function of the amplitude of the THz component, shown for each of the pulses shown in panels A-C. (For the case of the experimental THz waveform we simply scale the experimental data to change the amplitude). For all three pulses the spin current increases monotonically with A_0 showing control of current generation by THz amplitude, the key property of the hencomb pulse. For the pulses shown in panels A and B the full width half maxima are 56.5 fs, 141.3 fs. In each case the full width half maxima of the circularly polarized component is 42.4 fs with the frequency 2.20 eV (i.e. tuned to the gap). The maximal values of the peak electric field and peak power density are 0.34 MV/cm, 2.8 MV/cm, 2.9 MV/cm and 1×10^{10} W/cm^2.
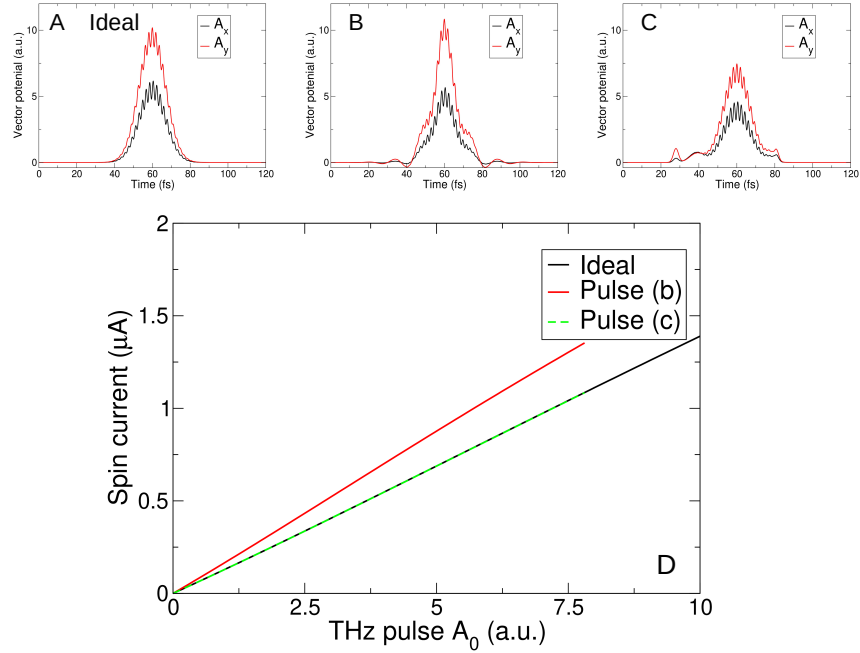
2.2   Pulse noise in hencomb pulses applied WSe$_2$

Figure S7: **Impact of pulse noise in the hencomb pulse as applied to WSe$_2$**. Panel A shows an ideal pulse, and panels B and C hencomb pulses with randomized noise frequencies added to the THz component. As shown in panel D in all cases the dependence of the spin current in WSe$_2$ on the amplitude of the THz component of the hencomb pulse is that of a monotonic increase, showing that this the key property of the hencomb pulse design holds also in the presence of noise components. The full width half maxima of each pulse component is 16.5 fs and the frequency of the circularly polarized components 2.20 eV (tuned to the gap).

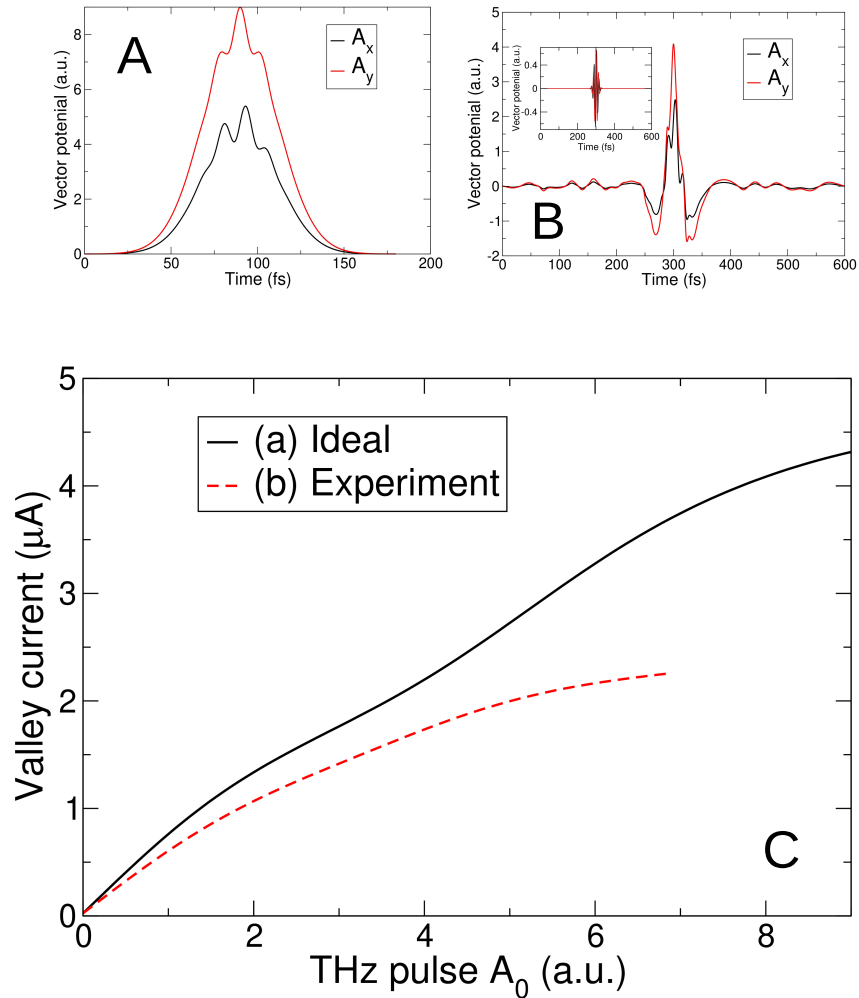## 2.3 Pulse noise in hencomb pulses applied to bilayer graphene

Figure S8: **Impact of pulse noise in the hencomb pulse as applied to bilayer graphene**. Panels A-B: vector potentials of two hencomb pulses applied to bilayer graphene with a gap of 300 meV: Panel A shows an ideal hencomb pulse and panel B a hencomb pulse in which the THz envelope is taken directly from experiment (Fig. 24 of Ref. 29). The inset displays the circularly polarized pulse added to the experimental THz envelope to create the hencomb pulse. As can be seen in panel C, the valley current generated depends monotonically on the amplitude of the THz component for both the ideal pulse and the hencomb pulse in which the THz envelope is taken from experiment, showing that control of current generation by the amplitude of the THz envelope – the key property of the hencomb pulse – is robust to the noisy and non-monocycle nature of typical experimental THz pulses. The full width half maxima are 23.5 fs and 49.5 fs of the circularly polarized and THz components respectively, the frequency of the circularly polarized component is 0.30 eV.

2.4 Pulse centre matching of linear THz and circular optical waveforms in the tungsten diselenide hencomb pulse
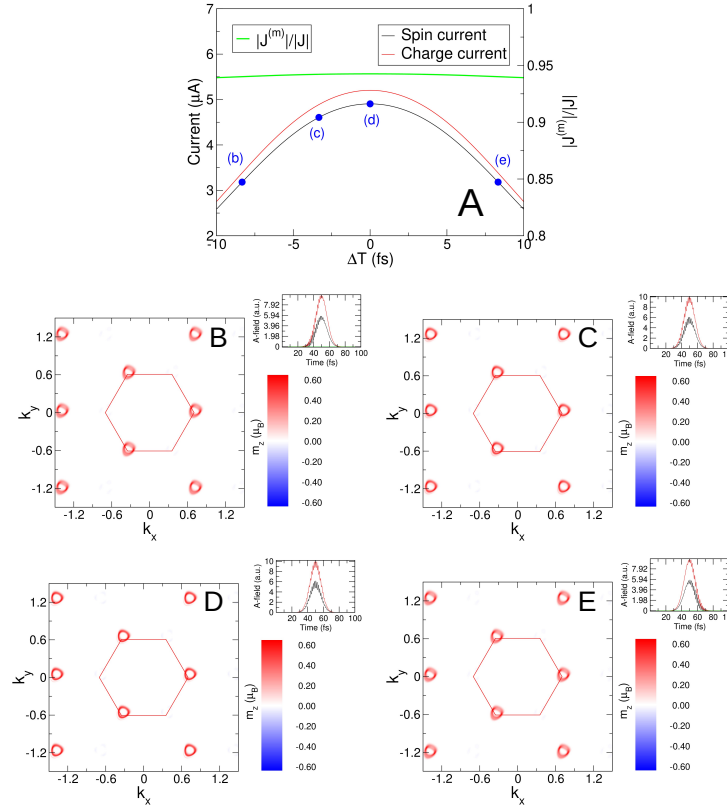

Figure S9: **Impact of pulse centre matching of the components of hencomb laser light on the spin current generated in WSe$_2$**. Panel A: impact of a mismatch ΔT between the temporal centres of the linearly polarized terahertz and circularly polarized optical light waveforms that constitute the hencomb pulse. A mismatch of up to 10 fs (69% of the full width half maximum of the circularly polarized component) preserves the effect but reduces the valley/spin current generated by $\sim 40\%$. There is almost no change in the valley/spin purity of the current, as can be seen from the ratio of spin $J^{(m)}$ to charge J currents $|J^{(m)}|/|J|$ referred to the left hand side axis. The vectors potentials and momentum space excitations of 4 representative cases are presented in panels B-E with the corresponding values of centre-mismatch indicated in panel A. As can be seen, the mismatch results in some blurring of the momentum space excitation which is sharpest for precise matching (panel D), but otherwise no significant change is observed.

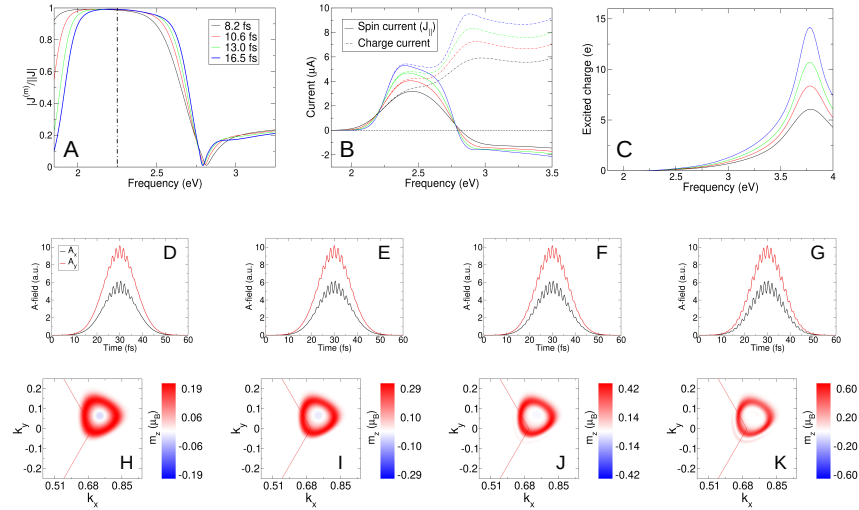## 2.5 Changing the full width half maximum of the circularly polarized component of the hencomb pulse

Figure S10: **Impact on valley/spin current and charge excitation from varying the full width half maximum (FWHM) of the circularly polarized optical component of the hencomb pulse.** The amplitude of the vector potential of the circularly polarized optical component is held fixed (vector potential 0.69 a.u.) and the THz component also held fixed (frequency 1 meV, vector potential 1.1 a.u., FWHM 14.5 fs). In panel A is shown the ratio of valley/spin to charge current, with the ratio nearly equal to 1 from frequencies close to the gap edge of 2.25 eV as indicated by the dashed vertical line. Decreasing the FWHM of the circularly polarized pulse component, as indicated by the caption, leads to some reduction of $|J^{(m)}|/|J|$ away from the gap edge, with no other significant impact on the qualitative form of the frequency dependence of the current response. As other pulse parameters are held fixed, increasing the FWHM results in an increase in current and excited charge, as shown in panels B and C. The vectors potentials and momentum space excitations for each FWHM considered, and for a frequency of 2.53 eV for the optical component, are shown in panels D-G and H-K respectively. As can be seen, a large FWHM leads to a much more localized momentum space excitation as the bandwidth of the frequency spectrum of the circularly polarized optical component narrows with increasing FWHM.

3 Convergence of intra- and inter-band current contributions

The current at time t can be written as

$$\mathbf{j}(t) = \sum_{\mathbf{q}} \langle \Psi_{\mathbf{q}}(t) | \boldsymbol{\nabla}_{\mathbf{p}} H(\mathbf{p}, t) | \Psi_{\mathbf{q}}(t) \rangle \tag{1}$$

$$|\Psi_{\mathbf{q}}(t)\rangle = \sum_{i} c_{i\mathbf{q}}(t) |\Phi_{i\mathbf{k}(t)}\rangle \tag{2}$$

$$\mathbf{k}(t) = \mathbf{q} - \mathbf{A}(t)/c \tag{3}$$

Taking the $\mathbf{p}$ derivative of the matrix element $\langle \Psi_{\mathbf{q}}(t) | H(\mathbf{p}, t) | \Psi_{\mathbf{q}}(t) \rangle$ leads directly to a separation into intra- and inter-band parts to the total current:
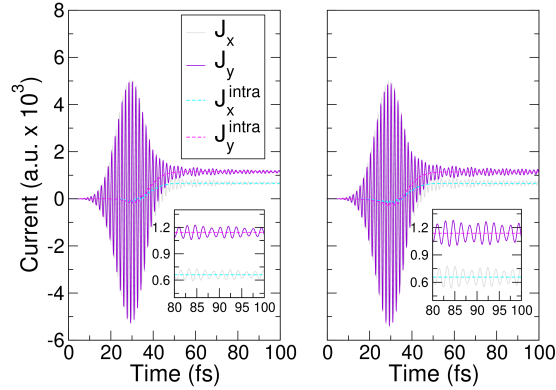

Figure S11: **Time dependence of the intraband (dashed line) and total current (full line) for a hencomb pulse**. The corresponding vector potential is shown in panel (a) of Fig. S12. The hencomb pulse parameters are $\omega = 2.52$ eV, vector potential 0.69 a.u. and a full width half maxima (FWHM) of 16.5 fs for the optical circularly polarized pulse component, and $\omega = 1$ meV, vector potential 1.1 a.u. and FWHM of 16.5 fs for the linearly polarized terahertz component. In panel A is shown the dynamics including the effects of decoherence with a decay time $T_{dco} = 200$ fs, while in panel B the dynamics are coherent. The effect of decoherence can be seen to result in a small reduction in the oscillation of the total current, due to the interband contribution, but almost no change on the intraband current.
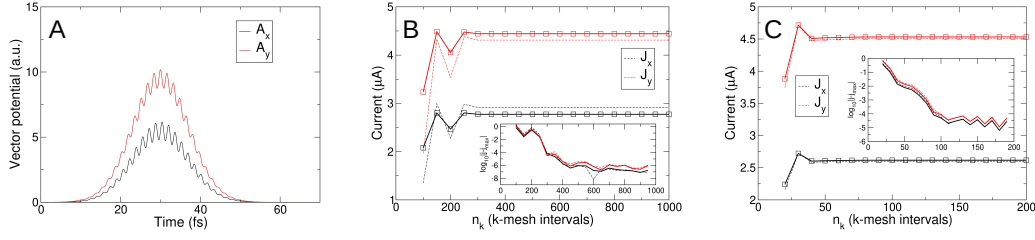
Figure S12: **Convergence of the total and intraband current**. The vector potential of the hencomb pulse displayed in panel A, and the hencomb pulse parameters are $\omega = 2.52$ eV, vector potential 0.69 a.u. and a full width half maxima (FWHM) of 16.5 fs for the optical circularly polarized pulse component, and $\omega = 1$ meV, vector potential 1.1 a.u. and FWHM of 16.5 fs for the linearly polarized terahertz component. The total current converges extremely slowly with increasing size of the $n_k \times n_k$ mesh, panel B; values of n_k greater than 400 are required for convergence. In dramatic contrast the dominant part of the total current, the intraband contribution, is reasonable converged already at around $n_k = 60$, panel C.

$$\mathbf{j}(t) = \mathbf{j}_{intra}(t) + \mathbf{j}_{inter}(t) \tag{4}$$

with

$$\mathbf{j}_{intra}(t) = \sum_{i\mathbf{q}} \left|c_{i\mathbf{k}(t)}\right|^2 \left|\boldsymbol{\nabla}_{\mathbf{p}}\epsilon_{i\mathbf{k}(t)}\right. \tag{5}$$

and

$$\mathbf{j}_{inter}(t) = -\sum_{ij} c^*_{i\mathbf{k}(t)}c_{j\mathbf{k}(t)}\epsilon_{j\mathbf{k}(t)} \left\langle \boldsymbol{\nabla}_{vp}\Phi_{i\mathbf{k}(t)} \middle| \Phi_{j\mathbf{k}(t)} \right\rangle + c.c. \tag{6}$$

The intra-band current, (5), will converge quickly as the size of k-mesh is increased, as the patterns of excited charge in momentum space induced by the hencomb pulse do not exhibit fine s tructure. H owever, t he i nterband c urrent, (6), c ontains p hase i nformation t hat rapidly oscillates in momentum space leading to a very slow convergence of the total current, (1). This can be seen in Fig. S12 in which is exhibited the converge of both the total (panel B) and the intraband current (panel C); while the former requires very high convergence exceeding grids

of 400×400, the latter is converged well already at 50×50.

4 Calculating intra-band current within time dependent density function theory

Time dependent density functional theory (TDDFT), Ref. 40-43, is an *ab-initio* method for solving the dynamics of many-electron systems via a computationally tractable non-interacting system, known as the Kohn-Sham (KS) system. The non-interacting time-dependent Kohn-Sham (TDKS) equation for periodic systems reads:

$$i\frac{\partial \phi_{j\mathbf{k}}(\mathbf{r}, t)}{\partial t} = \left[\frac{1}{2} \left(-i\boldsymbol{\nabla} + \frac{1}{c}\mathbf{A}_{\text{ext}}(t) \right)^2 + v_{\text{S}}(\mathbf{r}, t) + \frac{1}{2c}\boldsymbol{\sigma} \cdot \mathbf{B}_{\text{S}}(\mathbf{r}, t) \right.$$
$$\left. + \frac{1}{4c^2}\boldsymbol{\sigma} \cdot (\boldsymbol{\nabla} v_{\text{S}}(\mathbf{r}, t) \times -i\boldsymbol{\nabla}) \right] \phi_{j\mathbf{k}}(\mathbf{r}, t) \tag{7}$$

where $\phi_{j\mathbf{k}}(\mathbf{r}, t)$ are two-component Pauli spinor TDKS orbitals with quasi-momentum $\mathbf{k}$, $\mathbf{A}_{\text{ext}}(t)$ is the external laser field, written as a purely time-dependent vector potential, $\boldsymbol{\sigma}$ are the Pauli matrices, $v_{\text{S}}(\mathbf{r}, t) = v_{\text{ext}}(\mathbf{r}) + v_{\text{H}}(\mathbf{r}, t) + v_{\text{XC}}(\mathbf{r}, t)$ is the KS effective scalar potential, and $\mathbf{B}_{\text{S}}(\mathbf{r}, t) = \mathbf{B}_{\text{ext}}(\mathbf{r}, t) + \mathbf{B}_{\text{XC}}(\mathbf{r}, t)$ is the KS effective magnetic field. The external scalar potential, $v_{\text{ext}}(\mathbf{r})$, includes the electron-nuclei interaction, while $\mathbf{B}_{\text{ext}}(\mathbf{r}, t)$ is a external magnetic field which interacts with the electronic spins via the Zeeman interaction. The Hartree potential, $v_{\text{H}}(\mathbf{r}, t)$ is the classical electrostatic interaction. Finally we have the XC potentials, the scalar $v_{\text{XC}}(\mathbf{r}, t)$, and the XC magnetic field, $\mathbf{B}_{\text{XC}}(\mathbf{r}, t)$, which require approximation. In this work we used the adiabatic local density approximation (LDA).

The current is defined as:

$$J(t) = \sum_{j\mathbf{k}}^{occ} \langle \phi_{j\mathbf{k}}(t) | \hat{j} | \phi_{j\mathbf{k}}(t) \rangle \tag{8}$$

where $\hat{j}$ is standard quantum-mechanical current operator. Using the ground-state orbitals, $\varphi_{n\mathbf{k}}(\mathbf{r}, t)$, we can define the intraband current as:

$$J_{intra}(t) = \sum_{n\mathbf{k}} |c_{n\mathbf{k}}(t)|^2 \langle \varphi_{n\mathbf{k}} | \hat{j} | \varphi_{n\mathbf{k}} \rangle \tag{9}$$

where

$$c_{n\mathbf{k}}(t) = \sum_{j\mathbf{k}}^{occ} \langle \varphi_{n\mathbf{k}} | \phi_{j\mathbf{k}}(t) \rangle \tag{10}$$

is the projection of the TDKS orbitals into the ground-state orbitals.

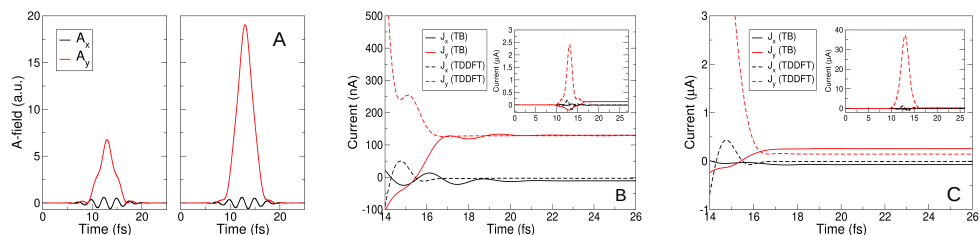# 5 Comparison of tight-binding and TD-DFT current

Figure S13: **Comparison between tight-binding model and TD-DFT residual currents for two femtosecond laser pulses**. The vector potentials are shown in panel A. For the smaller **A**-field pulse, panel B, the agreement for the residual current is nearly perfect. Comparison with the band structure in (see "Materials and Methods") shows that close to the K point, up to an energy shift due to the band gap error in LDA-DFT, the curvatures near the band edge are very similar. Further away from the band maximum however the TB band structure has a greater slope as compared to LDA-DFT leading, for the larger **A**-field pulse that explores these regions of momentum space, to a greater residual current from the TB calculation as compared to TD-DFT. During the pulse the different definitions of current – in TD-DFT only the paramagnetic contribution is considered – result in substantial differences between the currents (see inset graphs in panels B and C).